2009

Beam Spin Asymmetries in Deeply Virtual Compton Scattering (DVCS) With CLAS at 4.8 GeV

G. Gavalian
Old Dominion University

M. J. Amaryan
Old Dominion University, mamaryan@odu.edu

H. Bagdasaryan
Old Dominion University

M. Bektasoglu
Old Dominion University

S. Bültmann
Old Dominion University, sbueltma@odu.edu

See next page for additional authors

Authors
G. Gavalian, M. J. Amaryan, H. Bagdasaryan, M. Bektasoglu, S. Bültmann, S. L. Careccia, K. V. Dharmawardane, G. E. Dodge, N. Guler, C. E. Hyde, H. G. Juengst, N. Kalantarians, A. Klein, S. E. Kuhn, J. Lachniet, M. R. Niroula, R. A. Niyazov, L. M. Qin, F. Sabatié, S. Tkachenko, L. B. Weinstein, J. Yun, J. Zhang, and CLAS Collaboration

Beam spin asymmetries in deeply virtual Compton scattering (DVCS) with CLAS at 4.8 GeV

G. Gavalian,[1,2] V. D. Burkert,[3] L. Elouadrhiri,[3] M. Holtrop,[1] S. Stepanyan,[3] D. Abrahamyan,[19] G. Adams,[32] M. J. Amaryan,[2] P. Ambrozewicz,[15] M. Anghinolfi,[21] B. Asavapibhop,[27] G. Asryan,[40] H. Avakian,[3,20] H. Bagdasaryan,[2] N. Baillie,[39] J. P. Ball,[5] N. A. Baltzell,[35] S. Barrow,[16] V. Batourine,[25] M. Battaglieri,[21] K. Beard,[24] I. Bedlinskiy,[23] M. Bektasoglu,[2,30] M. Bellis,[8] N. Benmouna,[17] B. L. Berman,[17] A. S. Biselli,[14,32] B. E. Bonner,[33] S. Bouchigny,[3,22] S. Boiarinov,[3,23] R. Bradford,[8] D. Branford,[13] W. J. Briscoe,[17] W. K. Brooks,[3] S. Bültmann,[2] C. Butuceanu,[39] J. R. Calarco,[1] S. L. Careccia,[2] D. S. Carman,[3] B. Carnahan,[9] S. Chen,[16] P. L. Cole,[3,19] A. Coleman,[39,*] P. Collins,[5] P. Coltharp,[16] D. Cords,[3,†] P. Corvisiero,[21] D. Crabb,[38] H. Crannell,[9] V. Crede,[16] J. P. Cummings,[32] N. Dashyan,[40] R. De Masi,[10] R. De Vita,[21] E. De Sanctis,[20] P. V. Degtyarenko,[3] H. Denizli,[31] L. Dennis,[16] A. Deur,[3] K. V. Dharmawardane,[2] K. S. Dhuga,[17] R. Dickson,[8] C. Djalali,[35] G. E. Dodge,[2] J. Donnelly,[18] D. Doughty,[3,11] P. Dragovitsch,[16] M. Dugger,[5] S. Dytman,[31] O. P. Dzyubak,[35] H. Egiyan,[1,3] K. S. Egiyan,[40,‡] L. El Fassi,[4] A. Empl,[32] P. Eugenio,[16] R. Fatemi,[38] G. Fedotov,[28] G. Feldman,[17] R. J. Feuerbach,[8] T. A. Forest,[2] H. Funsten,[39] M. Garçon,[10] G. P. Gilfoyle,[34] K. L. Giovanetti,[24] F. X. Girod,[10] J. T. Goetz,[6] E. Golovatch,[21,28] A. Gonenc,[15] R. W. Gothe,[35] K. A. Griffioen,[39] M. Guidal,[22] M. Guillo,[35] N. Guler,[2] L. Guo,[3] V. Gyurjyan,[3] C. Hadjidakis,[22] K. Hafidi,[4] H. Hakobyan,[40] R. S. Hakobyan,[9] J. Hardie,[3,11] N. Hassall,[18] D. Heddle,[3,11] F. W. Hersman,[1] K. Hicks,[30] I. Hleiqawi,[30] J. Hu,[32] M. Huertas,[35] C. E. Hyde,[2,§] Y. Ilieva,[17] D. G. Ireland,[18] B. S. Ishkhanov,[28] E. L. Isupov,[28] M. M. Ito,[3] D. Jenkins,[37] H. S. Jo,[22] K. Joo,[12,38] H. G. Juengst,[2] N. Kalantarians,[2] J. D. Kellie,[18] M. Khandaker,[29] K. Y. Kim,[31] K. Kim,[25] W. Kim,[25] A. Klein,[2] F. J. Klein,[3,9] M. Klusman,[32] M. Kossov,[23] L. H. Kramer,[3,15] V. Kubarovsky,[3,32] J. Kuhn,[8] S. E. Kuhn,[2] S. V. Kuleshov,[23,25] M. Kuznetsov,[23,25] J. Lachniet,[2] J. M. Laget,[3,10] J. Langheinrich,[35] D. Lawrence,[27] A. C. S. Lima,[17] K. Livingston,[18] H. Y. Lu,[35] K. Lukashin,[3] M. MacCormick,[22] J. J. Manak,[3] N. Markov,[12] S. McAleer,[16] B. McKinnon,[18] J. W. C. McNabb,[8] B. A. Mecking,[3] M. D. Mestayer,[3] C. A. Meyer,[8] T. Mibe,[30] K. Mikhailov,[23] R. Minehart,[38] M. Mirazita,[20] R. Miskimen,[27] V. Mokeev,[28] K. Moriya,[8] S. A. Morrow,[10,22] M. Moteabbed,[15] J. Mueller,[31] G. S. Mutchler,[33] P. Nadel-Turonski,[17] J. Napolitano,[32] R. Nasseripour,[17] S. Niccolai,[17,22] G. Niculescu,[24,30] I. Niculescu,[17,24] B. B. Niczyporuk,[3] M. R. Niroula,[2] R. A. Niyazov,[2,3] M. Nozar,[3] G. V. O'Rielly,[17] M. Osipenko,[21,28] A. I. Ostrovidov,[16] K. Park,[25] E. Pasyuk,[5] C. Paterson,[18] S. A. Philips,[17] J. Pierce,[38] N. Pivnyuk,[23] D. Pocanic,[38] O. Pogorelko,[23] E. Polli,[20] I. Popa,[17] S. Pozdniakov,[23] B. M. Preedom,[35] J. W. Price,[7] Y. Prok,[26,38] D. Protopopescu,[18] L. M. Qin,[2] B. A. Raue,[3,15] G. Riccardi,[16] G. Ricco,[21] M. Ripani,[21] B. G. Ritchie,[5] F. Ronchetti,[20] G. Rosner,[18] P. Rossi,[20] D. Rowntree,[26] P. D. Rubin,[34] F. Sabatié,[2,10] J. Salamanca,[19] C. Salgado,[29] J. P. Santoro,[3,9] V. Sapunenko,[3,21] R. A. Schumacher,[8] V. S. Serov,[23] Y. G. Sharabian,[3] J. Shaw,[27] N. V. Shvedunov,[28] A. V. Skabelin,[26] E. S. Smith,[3] L. C. Smith,[38] D. I. Sober,[9] D. Sokhan,[13] A. Stavinsky,[23] S. S. Stepanyan,[25] B. E. Stokes,[16] P. Stoler,[32] I. I. Strakovsky,[17] S. Strauch,[35] R. Suleiman,[26] M. Taiuti,[21] S. Taylor,[33] D. J. Tedeschi,[35] U. Thoma,[3,‖] R. Thompson,[31] A. Tkabladze,[17,30] S. Tkachenko,[2] C. Tur,[35] M. Ungaro,[12,32] M. F. Vineyard,[34,36] A. V. Vlassov,[23] D. P. Watts,[18] L. B. Weinstein,[2] D. P. Weygand,[3] M. Williams,[8] E. Wolin,[3] M. H. Wood,[27,35] A. Yegneswaran,[3] J. Yun,[2] M. Yurov,[25] L. Zana,[1] J. Zhang,[2] B. Zhao,[12] and Z. W. Zhao[35]

(CLAS Collaboration)

[1]*University of New Hampshire, Durham, New Hampshire 03824-3568, USA*
[2]*Old Dominion University, Norfolk, Virginia 23529, USA*
[3]*Thomas Jefferson National Accelerator Facility, Newport News, Virginia 23606, USA*
[4]*Argonne National Laboratory, Argonne, Illinois 60439, USA*
[5]*Arizona State University, Tempe, Arizona 85287-1504, USA*
[6]*University of California at Los Angeles, Los Angeles, California 90095-1547, USA*
[7]*California State University, Dominguez Hills, Carson, California 90747, USA*
[8]*Carnegie Mellon University, Pittsburgh, Pennsylvania 15213, USA*
[9]*Catholic University of America, Washington, DC 20064, USA*
[10]*CEA-Saclay, Service de Physique Nucléaire, F-91191 Gif-sur-Yvette, France*
[11]*Christopher Newport University, Newport News, Virginia 23606, USA*
[12]*University of Connecticut, Storrs, Connecticut 06269, USA*
[13]*Edinburgh University, Edinburgh EH9 3JZ, United Kingdom*
[14]*Fairfield University, Fairfield Connecticut 06824, USA*
[15]*Florida International University, Miami, Florida 33199, USA*
[16]*Florida State University, Tallahassee, Florida 32306, USA*
[17]*The George Washington University, Washington, DC 20052, USA*
[18]*University of Glasgow, Glasgow G12 8QQ, United Kingdom*
[19]*Idaho State University, Pocatello, Idaho 83209, USA*
[20]*INFN, Laboratori Nazionali di Frascati, I-00044 Frascati, Italy*
[21]*INFN, Sezione di Genova, I-16146 Genova, Italy*
[22]*Institut de Physique Nucleaire ORSAY, Orsay, France*
[23]*Institute of Theoretical and Experimental Physics, Moscow RU-117259, Russia*
[24]*James Madison University, Harrisonburg, Virginia 22807, USA*
[25]*Kyungpook National University, Daegu 702-701, Republic of Korea*

[26]*Massachusetts Institute of Technology, Cambridge, Massachusetts 02139, USA*
[27]*University of Massachusetts, Amherst, Massachusetts 01003, USA*
[28]*Moscow State University, General Nuclear Physics Institute, RU-119899 Moscow, Russia*
[29]*Norfolk State University, Norfolk, Virginia 23504, USA*
[30]*Ohio University, Athens, Ohio 45701, USA*
[31]*University of Pittsburgh, Pittsburgh, Pennsylvania 15260, USA*
[32]*Rensselaer Polytechnic Institute, Troy, New York 12180, USA*
[33]*Rice University, Houston, Texas 77005, USA*
[34]*University of Richmond, Richmond, Virginia 23173, USA*
[35]*University of South Carolina, Columbia, South Carolina 29208, USA*
[36]*Union College, Schenectady, New York 12308, USA*
[37]*Virginia Polytechnic Institute and State University, Blacksburg, Virginia 24061, USA*
[38]*University of Virginia, Charlottesville, Virginia 22901, USA*
[39]*College of William and Mary, Williamsburg, Virginia 23187, USA*
[40]*Yerevan Physics Institute, 375036 Yerevan, Armenia*
(Received 26 January 2009; published 29 September 2009)

We report measurements of the beam spin asymmetry in deeply virtual Compton scattering (DVCS) at an electron beam energy of 4.8 GeV using the CLAS detector at the Thomas Jefferson National Accelerator Facility. The DVCS beam spin asymmetry has been measured in a wide range of kinematics, $1.0 < Q^2 < 2.8\ (\mathrm{GeV}/c)^2$, $0.12 < x_B < 0.48$, and $0.1 < -t < 0.8\ (\mathrm{GeV}/c)^2$, using the reaction $\vec{e}p \to e'pX$. The number of H$(e, e'\gamma p)$ and H$(e, e'\pi^0 p)$ events are separated in each (Q^2, x_B, t) bin by a fit to the line shape of the H$(e, e'p)X$ M_x^2 distribution. The validity of the method was studied in detail using experimental and simulated data. It was shown that with the achieved missing mass squared resolution and the available statistics, the separation of DVCS–Bethe-Heitler and π^0 events can reliably be done with less than 5% uncertainty. Also, the Q^2 and t dependences of the $\sin\phi$ moments of the asymmetry are extracted and compared with theoretical calculations.

DOI: 10.1103/PhysRevC.80.035206 PACS number(s): 13.60.Fz, 14.20.Dh, 24.70.+s, 24.85.+p

I. INTRODUCTION

Hard scattering processes play an important role in the understanding of the quark and gluon structure of hadrons. The important feature of hard reactions is the possibility of separating the perturbative (short distance) and nonperturbative (long distance) parts of the interaction. This so-called factorization property has been successfully used in inclusive measurements [e.g., in deep inelastic scattering (DIS) of leptons] to study the internal structure of the nucleon. Until recently, very few exclusive processes could be treated in the framework of perturbative QCD (pQCD) and compared to experimental data (typical examples are the $\pi^0\gamma\gamma^*$ transition form factor [1] and the elastic form factors of the pion [2] and the nucleon [3]). The recently developed formalism of a QCD description of deeply virtual Compton scattering (DVCS) [4,5] and deeply exclusive meson production [6] provides a framework in which the amplitudes of these processes can be factorized into a hard-scattering part (exactly calculable in pQCD) and a nonperturbative nucleon structure part that can be parametrized at the amplitude level by means of generalized parton distributions (GPDs). The GPDs contain information on quark/antiquark correlations, particularly the correlation of their transverse spatial and longitudinal momentum distributions, and on the quark angular momentum [7]. They provide a unifying picture for an entire set of fundamental quantities containing information on the hadronic structure, such as nucleon form factors (which are related to matrix elements of vector and axial vector currents), polarized and unpolarized parton distributions, and contributions to the spin of the nucleon due to orbital excitations of quarks and gluons.

There are four chiral-even GPDs, denoted H^q, $\tilde{H}^q$, E^q, and $\tilde{E}^q$, which depend on the kinematical variables x, ξ, and t. They correspond to the amplitude for removing a quark with momentum fraction $x + \xi$ and restoring it with momentum fraction $x - \xi$. The light-cone momentum fraction x is defined by $k^+ = x\bar{P}^+$, where k is the quark loop momentum and $\bar{P}$ is the average nucleon momentum [$\bar{P} = (p' + p)/2$, where p and p' are the initial and final state nucleon four-momenta, respectively]. ξ is the generalized Bjorken variable, $\xi = Q^2/(4q \cdot \bar{P}) \to x_B/(2 - x_B)$ as $t/Q^2 \to 0$, where $q = k - k'$ and $Q^2 = -q^2$. k and k' are the initial and final electron momenta.

The Mandelstam variable $t = \Delta^2 = (p' - p)^2$ is the Lorentz-invariant four-momentum transfer squared to the target. In the forward limit, $t \to 0$, the GPDs H and $\tilde{H}$ reduce to the quark density distributions $q(x)$ and quark helicity

[*]Current address: Systems Planning and Analysis, Alexandria, Virginia 22311, USA.
[†]Deceased.
[‡]Deceased.
[§]Current address: Université Blaise Pascal/CNR-IN2P3, F-63177 Aubière, France.
[‖]Current address: Physikalisches Institut der Universitaet Giessen, D-35392 Giessen, Germany.

distributions $\Delta q(x)$ obtained from DIS:

$$H^q(x,0,0) = \begin{cases} q(x), & x > 0, \\ -\bar{q}(-x), & x < 0, \end{cases} \tag{1}$$

$$\tilde{H}^q(x,0,0) = \begin{cases} \Delta q(x), & x > 0, \\ \Delta\bar{q}(-x), & x < 0. \end{cases} \tag{2}$$

E and $\tilde{E}$ are accessible only through hard exclusive electroproduction reactions and are new leading-twist functions. Similarly, in DIS, which corresponds to the limit $\xi \to 0$, the region $-\xi < x < \xi$ is absent. In this region the GPDs behave like meson distribution amplitudes and contain completely new information about nucleon structure. At finite momentum transfer, the first moments of the GPDs are related to the elastic form factors of the nucleon through model-independent sum rules. By integrating over x, one can obtain for a particular quark flavor (for any ξ)

$$\int_{-1}^{+1} dx\, H^q(x,\xi,t) = F_1^q(t), \tag{3}$$

$$\int_{-1}^{+1} dx\, E^q(x,\xi,t) = F_2^q(t), \tag{4}$$

$$\int_{-1}^{+1} dx\, \tilde{H}^q(x,\xi,t) = g_A^q(t), \tag{5}$$

$$\int_{-1}^{+1} dx\, \tilde{E}^q(x,\xi,t) = h_A^q(t), \tag{6}$$

where $F_1^q(t)$ and $F_2^q(t)$ represent the elastic Dirac and Pauli form factors, respectively, for the quark flavor q in the nucleon, g_A^q is the axial-vector form factor of the nucleon, and h_A^q is the pseudoscalar form factor.

Deeply virtual Compton scattering (DVCS), $ep \to ep\gamma$, is the simplest reaction to access GPDs experimentally. DVCS has the same final state as the Bethe-Heitler (BH) process, where a photon is emitted by the incoming or outgoing electron (Fig. 1). The differential cross section for the process $ep \to ep\gamma$ can be written as [8]

$$\frac{d\sigma}{dx_B\, dy\, dt\, d\phi} = \frac{\alpha^3 x_B y}{8\pi\, Q^2\sqrt{1+\epsilon^2}} |\mathcal{T}|^2. \tag{7}$$

Here the amplitude of the production of a real photon, $\mathcal{T}$, is the sum of the DVCS ($\mathcal{T}_{\rm DVCS}$) and BH ($\mathcal{T}_{\rm BH}$) amplitudes, given as

$$\mathcal{T}^2 = |\mathcal{T}_{\rm BH}|^2 + |\mathcal{T}_{\rm DVCS}|^2 + \mathcal{I}, \tag{8}$$

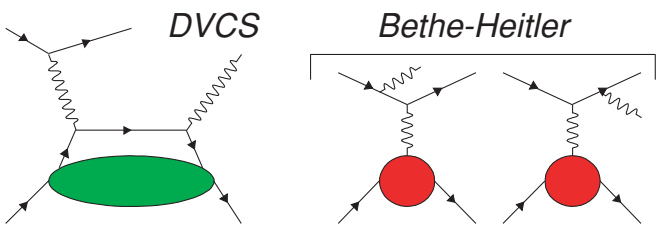

FIG. 1. (Color online) Feynman diagrams for DVCS and Bethe-Heitler processes contributing to the amplitude of $ep \to e'p\gamma$ scattering.

where

$$\mathcal{I} = \mathcal{T}_{\rm DVCS}\mathcal{T}_{\rm BH}^* + \mathcal{T}_{\rm DVCS}^*\mathcal{T}_{\rm BH} \tag{9}$$

is the interference term. $\mathcal{T}_{\rm BH}$ is real to the lowest order in the QED fine structure constant α. The lepton energy fraction y and Bjorken variable x_B are defined as

$$y = \frac{p\cdot q}{p\cdot k}, \quad x_B = \frac{Q^2}{2p\cdot q}. \tag{10}$$

In the notation of Ref. [8], $\epsilon = 2x_B M/Q$, where M is the nucleon mass. ϕ is the angle between the leptonic plane and the proton-photon production plane.

Contraction of the leptonic and hadronic tensors generates an azimuthal angular dependence of each of the three terms in Eq. (8) [10]. In a frame with the z axis along the virtual photon, the dependence of the amplitudes on ϕ yields a finite sum of Fourier harmonics. The amplitude of deeply virtual production of a photon has been derived up to twist-3 accuracy [8]. In the notation of Ref. [8], the helicity-dependent angular moments are presented in a series of $\sin(n\phi)$, with $n = 1, 2, 3$. Only $n = 1$ is a twist-2 quark matrix element. The $n = 2$ terms are twist-3 and the $n = 3$ terms are twist-2 double-helicity-flip gluon transversity terms, which are kinematically suppressed. If these terms are omitted, then at the twist-2 level, the BH, DVCS, and interference contributions to the total cross section in Eq. (8) read

$$|\mathcal{T}_{\rm BH}|^2 = \frac{1}{x_B^2 y^2(1+\epsilon^2)^2\Delta^2\,\mathcal{P}_1(\phi)\mathcal{P}_2(\phi)} \times \left\{c_0^{\rm BH} + c_1^{\rm BH}\cos\phi + c_2^{\rm BH}\cos 2\phi\right\}, \tag{11}$$

$$|\mathcal{T}_{\rm DVCS}|^2 = \frac{1}{y^2Q^2}\left\{c_0^{\rm DVCS}\right\}, \tag{12}$$

$$\mathcal{I} = \frac{-1}{x_B y^3\Delta^2\mathcal{P}_1(\phi)\mathcal{P}_2(\phi)} \times \left\{c_0^{\mathcal{I}} + c_1^{\mathcal{I}}\cos\phi + s_1^{\mathcal{I}}\sin\phi\right\}, \tag{13}$$

where $\mathcal{P}_1(\phi)$ and $\mathcal{P}_2(\phi)$ are the BH propagators.

Experimentally, the simplest observable to measure GPDs is the beam spin asymmetry ($A_{\rm LU}$). The largest contribution to this observable arises from the imaginary part of the interference of the DVCS and the BH amplitudes, $s_1^{\mathcal{I}}$. $s_1^{\mathcal{I}}$ is the most interesting Fourier harmonic since it is linear in the Compton form factor (CFF), that is,

$$s_1^{\mathcal{I}} = 8K\lambda y(2-y)\Im{\rm m}[C^I(\mathcal{F})], \tag{14}$$

where K is the $\sqrt{-t/Q^2}$ power-suppressed kinematical factor and λ is the beam polarization.[1] Thus, at the twist-2 level, the helicity-dependent cross-section difference will be

$$A_{\rm LU}(\phi)\cdot(\sigma^+ + \sigma^-) = \sigma^+ - \sigma^- = \frac{-16Ky(2-y)}{x_B y^3\Delta^2\mathcal{P}_1(\phi)\mathcal{P}_2(\phi)} \times \left(F_1\mathcal{H} + \frac{x_B}{2-x_B}(F_1+F_2)\tilde{\mathcal{H}} - \frac{t}{4M^2}F_2\mathcal{E}\right)\sin\phi. \tag{15}$$

[1]Note that power-suppressed contributions not included in Ref. [8] could modify Eqs. (14) and (15) [9].

Measuring the imaginary part of the CFF $[\mathcal{H}, \tilde{\mathcal{H}}, \mathcal{E}]$ gives access to the GPDs $[H, \tilde{H}, E]$ at the specific kinematical point $x = \xi$. From a phenomenological point of view, the extraction of the GPDs from data requires an extensive experimental program and detailed analysis with controlled theoretical corrections. This field is rapidly expanding (see, e.g., Refs. [11–13]); and as a first step, the phenomenological parametrization of GPDs is used to fit the experimental data.

The azimuthal dependence of the beam spin asymmetry has been measured by the CLAS [14] and HERMES [15] Collaborations with electron (4.25 GeV) and positron (27.6 GeV) beams, respectively. The longitudinal target-spin asymmetry has been reported by CLAS [16]. The Q^2 dependence of the helicity-dependent and helicity-independent cross sections was measured by the Hall A Collaboration at Jefferson Lab [17]. The beam charge asymmetry [18] and transverse target-spin asymmetry [19] have also been reported by the HERMES Collaboration. Recently, the CLAS Collaboration published measurements of the DVCS beam spin asymmetry over a wide kinematical range using high statistics data obtained with a 5.77 GeV longitudinally polarized electron beam [20]. In this paper, new results on the beam spin asymmetry in DVCS at 4.8 GeV using the CLAS detector are presented. Measuring the same observables at the same (x_B, Q^2, t) but different energies will yield different combinations of the terms of interest and thus contribute to the determination of GPDs. In this analysis, the number of single photon events has been extracted using the method developed in Ref. [14]. A fit to the line shape of the missing mass squared distributions in the reaction $\vec{e}p \to epX$ was employed in each kinematical bin. The Q^2 and t dependences of the $\sin\phi$ moments have been extracted and are compared with theoretical predictions.

II. EXPERIMENT

The measurement was carried out using the Continuous Electron Beam Accelerator Facility (CEBAF) large acceptance spectrometer (CLAS) detector [21] in Hall B at the Thomas Jefferson National Accelerator Facility. The CLAS detector system is based on a toroidal magnet that consists of six superconducting coils. The coils are positioned symmetrically around the beamline and provide a toroidal field in the azimuthal direction. Each of the gaps between the coils is instrumented with an identical detector package covering typically 80% of 2π in the azimuthal direction.

The CLAS detector package includes three regions of drift chambers (DCs) and a set of scintillator counters (SCs) for the tracking and identification of long-lived charged particles using the time-of-flight technique. The DCs and SCs cover the laboratory polar angular range from 8° to 140°. In the forward region, CLAS has gas threshold Cherenkov counters (CCs) and electromagnetic calorimeters (ECs) for electron identification. The ECs are also used for detection and identification of photons and neutrons. The momentum resolution of the system is approximately 1%. The efficiency of single charged-particle detection is $\geqslant$95% in the fiducial volume of the detector.

The data used in this analysis were taken during February and March of 2000. The 4.8 GeV longitudinally polarized electron beam was incident on a 5-cm-long liquid-hydrogen target. The average beam current was 5 nA. The total integrated luminosity was 1.28 fb^{-1}. The CLAS data acquisition system (DAQ) was triggered by a coincidence of signals from the CCs and the ECs. The DAQ rate was 1.1 kHz at 95% live time. The beam polarization was measured several times during the run using the Hall B Moller polarimeter. The average polarization was 70% with an uncertainty of $\pm$3%.

A total of 1.26×10^6 triggers have been processed, of which about 18% contained a properly identified electron. For the physics analysis, events with only one detected electron and one detected proton were used. For systematic checks, the final states $(ep\gamma)$ and $(ep\gamma\gamma)$ were analyzed.

III. PARTICLE IDENTIFICATION

At the initial stage of data processing, the three-momenta of all final state particles are defined and preliminary particle identification (PID) is performed. Later, in the physics analysis, these PIDs are refined using the knowledge of the event kinematics.

For the identification of electrons, the energy deposited in the EC and the number of photoelectrons detected in the CC are used. This method relies on the correct reconstruction of the shower energy and on the analysis of the electromagnetic shower profile. Fiducial cuts in the calorimeter plane are used to reject particles that pass close to the edges and lose part of their energy outside of the calorimeter detection volume. In Fig. 2, the distribution of the number of photoelectrons detected in the CC, $N_{\text{p.e.}}$, vs the ratio $\Delta E_{\text{EC}}/P$ is shown after the fiducial cuts have been applied. Here ΔE_{EC} is the electromagnetic shower energy detected in the EC and P is the momentum of the particle reconstructed in the DC. The lower horizontal band corresponds to negative pions. The vertical band, centered at $\Delta E_{\text{EC}}/P \simeq 0.27$ (average electromagnetic shower energy sampling fraction of the EC), corresponds to electrons. A cut $N_{\text{p.e.}} > 2.5$ is used to reject most of the pions. Then, the distribution $\Delta E_{\text{EC}}/P$ is fitted by a Gaussian function and a $\pm 3\sigma$ cut around the mean is imposed to further clean the electron sample.

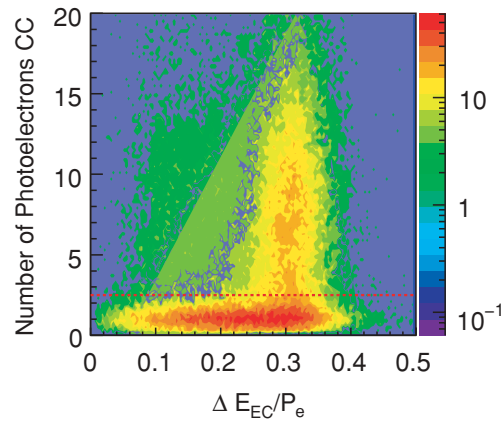

FIG. 2. (Color online) Distribution of the number of photoelectrons detected in the CC vs the sampling fraction of the EC.

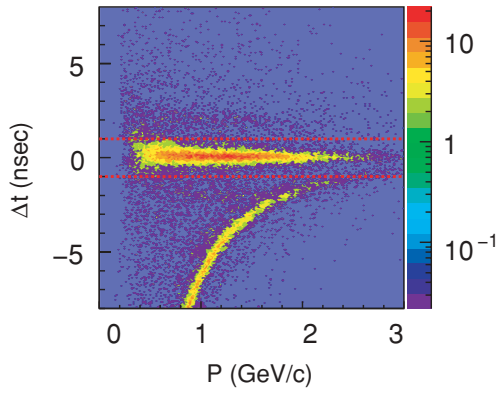

FIG. 3. (Color online) Vertex time distribution as a function of momentum for positive tracks. The particle velocity is deduced from the momentum using the proton mass.

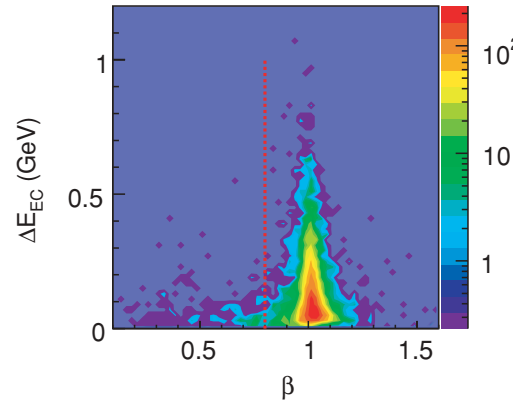

FIG. 4. (Color online) Distribution of the energy measured in the EC vs β for neutral particles detected in the EC. The vertical band at $\beta = 1$ corresponds to photons.

Momentum and time-of-flight (TOF) analyses are performed to identify protons. The CLAS TOF system allows the separation of protons from kaons up to 2 GeV/c and protons from pions up to 3 GeV/c momentum. In the kinematics of this analysis, protons have momenta smaller than 1 GeV/c. Protons are selected using a cut on the vertex time, Δt, calculated by

$$\Delta t = t - R/\beta - t_s. \tag{16}$$

Here, t is the time measured in the SC and R is the track length from the production vertex to the scintillator plane, which is determined by the tracking routines. In Eq. (16), $\beta = p/\sqrt{p^2 + m^2}$, where p and m are the proton momentum and rest mass. The event start time t_s is defined by the electron in the event as $t_s = t_e - R_e/c$, where t_e is the time measured in the SC for the electron track and R_e is the electron track length from the production vertex to the scintillator plane. In Fig. 3, the dependence of Δt on the momentum is presented for positively charged particles assuming they are protons. The horizontal band centered at 0 ns corresponds to protons. The lower band, emerging from negative Δt and closing to the proton band at high momentum, corresponds to positive pions. A ± 1 ns cut, shown by the dashed lines, is used to select protons.

While final beam spin asymmetries for DVCS-BH events were obtained using fits to the missing mass distributions in the reaction $ep \to epX$, events with $ep\gamma$ and $ep\gamma\gamma$ are used to extract the fit parameters and to study systematic uncertainties. The neutral particles in CLAS are detected and identified in the electromagnetic calorimeter. Neutrons and photons in the EC are separated by analyzing the speed of the neutral hits ($\beta_{\rm EC}$). For the selection of photons, a cut on $\beta_{\rm EC} > 0.85$ is used, see Fig. 4. The energy of the photon is reconstructed using the energy deposited in the EC, corrected for the sampling fraction of the calorimeter of 0.27.

IV. KINEMATIC CORRECTIONS

Two types of corrections have been applied to the measured momenta of electrons and protons. The first one is a correction to the proton momentum to account for energy loss in the material of the target and in the CLAS detector. The second one is a correction to account for small uncertainties in the magnetic field map and in the drift chamber alignment.

The energy loss corrections for protons are derived using the GEANT simulation package for the CLAS detector. Protons are simulated in the kinematic region covered by the experimental data. The ratio of the generated over the reconstructed momenta is parametrized as a function of the reconstructed momentum using a polynomial function. This function is then used to correct the measured momentum in the analysis of the experimental data.

To correct for the effects of the DC misalignments and the uncertainties in the magnetic field distribution, two methods, applied to kinematically complete reactions, were studied. The first method corrects only the magnitude of the electron and proton momenta. In the second method, a complex fitting algorithm is used to derive corrections for momenta and angles of all charged particles in an exclusive event. These corrections depend on the momentum, angle, and charge of the final state particle and do not depend on the particle type.

In the first method, the electron momentum corrections are derived using the Bethe-Heitler (BH) events associated with radiation of an energetic photon by the incoming electron. The kinematics of the secondary electrons in such events are similar to the kinematics in the deep inelastic scattering regime. For the selection of the BH events, cuts on the missing mass squared, on the transverse component of the missing momentum, and on the difference of azimuthal angles of the electron (ϕ_e) and the proton (ϕ_p) in the reaction $ep \to epX$ are used. In Fig. 5(a), the missing transverse momentum distribution is shown for events with the missing mass squared within ± 0.1 (GeV/c^2)^2. The corresponding distribution for the azimuthal angle difference, $|\phi_e - \phi_p|$, is shown in Fig. 5(b) with a dashed line histogram. A cut $\sqrt{(P_m^x)^2 + (P_m^y)^2}/P_m < 0.01$ has been applied to select events with missing momentum in the direction of the beam (the radiated photon is in the direction of the incoming electron). Here P_m is the magnitude and P_m^x and P_m^y are the transverse components of the missing momentum. In Fig. 5(b), the solid line histogram corresponds to the azimuthal angle difference after the cut on the transverse component of the missing momentum. The distribution peaks

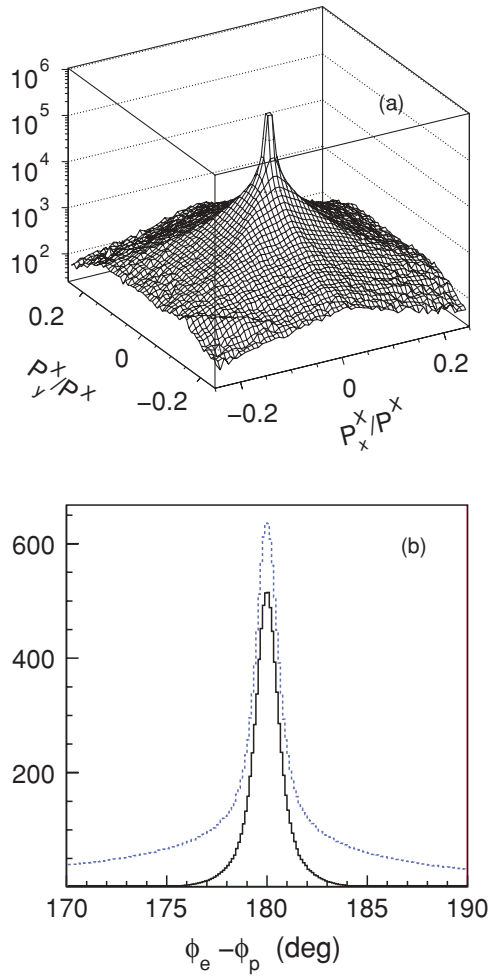

FIG. 5. (Color online) Selection of the BH events. (a) Distribution of the x and y components of the missing momentum. The strong peak at zero corresponds to BH events. (b) Electron and proton azimuthal angle difference before (dashed line histogram) and after (solid line histogram) the cut on the x and y components of the missing momentum.

at 180°, as it should for the elastic scattering events. A cut $178^\circ < |\phi_e - \phi_p| < 182^\circ$ was used to select the final event sample.

The scattered electron momentum P_f^e was calculated using the measured polar angles:

$$P_f^e = \frac{P_i^e}{1 + \frac{P_i^e}{M}(1 - \cos\theta_e)},$$
$$P_i^e = \frac{M}{1 - \cos\theta_e}\left(\cos\theta_e + \cos\theta_p \frac{\sin\theta_e}{\sin\theta_p} - 1\right), \quad (17)$$

where θ_e and θ_p are the polar angles of the electron and the proton, respectively, and M is the proton mass. P_i^e is the energy of the interacting electron after radiation. The ratio of P_f^e over the measured momentum was parametrized as a function of the measured angles and momenta and used as a correction factor to the measured electron momentum.

For the proton momentum, corrections derived for the π^+ from the reaction $ep \to en\pi^+$ with a missing neutron are used. The $e\pi^+ n$ events are selected using a $\pm 3\sigma$ cut around the neutron mass peak. The pion momentum was calculated after applying corrections to the electron momentum and from the assumption that the missing particle is a neutron. As above, the ratio of the calculated and measured momenta was parametrized as a function of the measured angles and momenta and used as a correction factor.

In the second method, we used the Bethe-Heitler and π^0 production events. The BH events are selected in the same way as above. To identify the pion events, two photons, in addition to an electron and a proton, have to be detected. A cut on the invariant mass of the two photons was used for the final selection of π^0 events. Using the missing mass squared of the photon and π^0 as a constraint in the fit, corrections for the momenta and polar angles of the electron and the proton are derived.

Both methods give comparable results. For the final analysis, corrections obtained by the second method are used. In Fig. 6(a), the missing mass squared distribution for BH

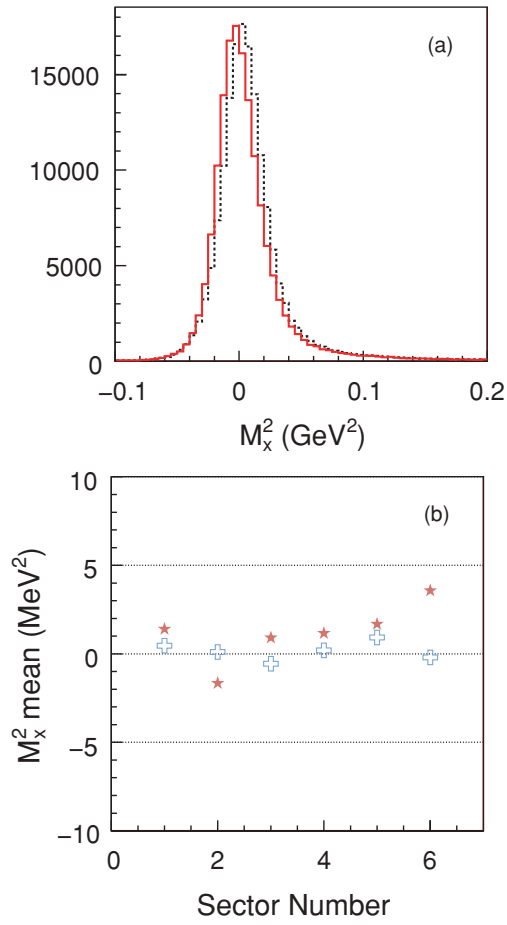

FIG. 6. (Color online) (a) Missing mass squared of $ep \to epX$ for the BH events before (dashed line histogram) and after (solid line histogram) momentum corrections are applied. (b) Dependence of the Gaussian means of the missing mass squared distributions on the CLAS sector before (stars) and after (crosses) the momentum corrections.

events is shown before (dashed line histogram) and after (solid line histogram) corrections are applied. After corrections are applied, the position of the missing mass peak has moved to the correct value and the width of the peak has improved. In Fig. 6(b), the improvement on the mean values of the missing mass (M_x^2) distributions of BH events as a function of CLAS sector are shown. The variation of the centroids is less than 0.001 GeV^2 after momentum corrections.

V. DVCS ANALYSIS

The beam spin asymmetry in DVCS is studied in the kinematical region of $W > 2$ GeV and $1.4 < Q^2 < 2.8$ (GeV/c)^2 using the reaction $ep \to e'pX$ where only one electron and one proton are detected in CLAS. The kinematical coverage is shown in Fig. 7.

The azimuthal angular modulations of the beam spin asymmetry ($A_{\rm LU}$) were extracted for three bins in Q^2, shown with horizontal lines in the left graph of Fig. 7, for the transferred momentum range from 0.1 to 0.4 (GeV/c)^2. The t dependence of the angular modulations have been studied in three bins of t, shown by the vertical lines in the right graph, for the Q^2 range from 1.4 to 2.5 (GeV/c)^2.

For each Q^2 and t bin, the data were divided into 11 bins of $\phi_{p\gamma}$, the azimuthal angle of the proton-photon production plane to the electron scattering plane (see Fig. 8). Note that in our notation, ϕ is defined as $\phi = \pi - \phi_{p\gamma}$. In each kinematical bin, the number of $\vec{e}p \to e'p\gamma$ events for positive (N_γ^+) and negative (N_γ^-) helicity states of the beam electrons and for the helicity sum (N_γ) have been extracted using a fit to the line shape of the missing mass squared distributions. The beam spin asymmetry was calculated as

$$A_{\rm LU} = \frac{1}{P_e} \cdot \frac{N_\gamma^+ - N_\gamma^-}{N_\gamma}, \tag{18}$$

where P_e is the average polarization of the beam. The helicity-related charge asymmetry has been measured using the inclusive electron yield. It was found to be 0.7% and is included in the estimation of the systematic uncertainties.

After omitting terms suppressed by an order of $-t/Q^2$ or higher in Eqs. (11)– (13) and (15), $A_{\rm LU}$ can be written as

$$A_{\rm LU} = \frac{\alpha' \sin\phi}{1 + \gamma\cos\phi}, \tag{19}$$

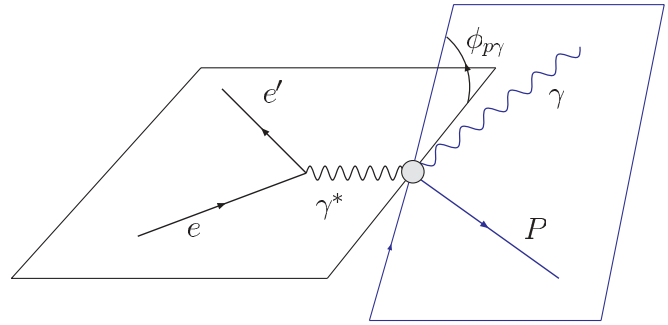

FIG. 8. (Color online) Kinematics of electroproduction in the target rest frame. The azimuthal angle $\phi_{p\gamma}$ is the angle between the proton-photon production plane and the electron scattering plane. The azimuthal angle defined in Ref. [8] and presented in Eq. (15) is $\phi = \pi - \phi_{p\gamma}$.

where the coefficients α' and γ are

$$\alpha' = \frac{x_B}{y}(1+\epsilon^2)^2 \frac{s_1^{\mathcal{I}}}{c_0^{\rm BH}}, \tag{20}$$

$$\gamma = \frac{y c_1^{\rm BH} + x_B(1+\epsilon^2)^2 c_1^{\mathcal{I}}}{y c_0^{\rm BH}}. \tag{21}$$

In our analysis, the $\sin\phi_{p\gamma}$ moment of $A_{\rm LU}$, which is a linear combination of GPDs [see Eq. (15)], has been extracted in each Q^2 and t bin using fits to the $\phi_{p\gamma}$ dependence of $A_{\rm LU}$ with the function

$$A_{\rm LU} = \alpha \sin\phi_{p\gamma} + \beta \sin 2\phi_{p\gamma}. \tag{22}$$

In this representation, all the higher order terms in the azimuthal angle have been combined in the parameter β. Note that power-suppressed contributions could modify Eqs. (14) and (15) [9].

A. Missing mass technique

The main challenge in the DVCS analysis using the reaction $ep \to e'pX$ is the separation of the single photon events from the more than one photon events, mostly π^0. In the kinematics of deep inelastic scattering, the CLAS resolution of the missing mass squared is not sufficient to separate these two final states cleanly. For the separation of $ep\gamma$ and $ep\gamma\gamma$ events, a fit to the line shape of the missing mass squared distribution is used. This technique for the extraction of the

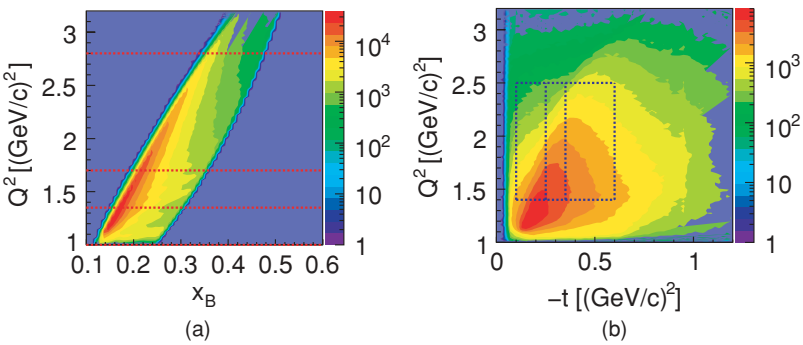

FIG. 7. (Color online) Kinematical coverage of the data set. (a) Q^2 vs x_B distribution with our Q^2 bin divisions. (b) Q^2 vs t distribution. The boxes indicate the kinematical bins used for this analysis (see Tables III and IV).

DVCS information in the reaction $ep \to e'pX$ has already been used in the DVCS analysis of the CLAS data at 4.2 GeV beam energy [14]. The high statistics of this data set and the comprehensive simulation enable detailed studies of the systematic uncertainties associated with the missing mass technique.

The main contributions to the missing mass squared distribution in the range $-0.1 < M_x^2 < 0.2$ GeV/c^2 come from three processes: (1) single photon production, (2) π^0 production, and (3) radiative processes associated with photon and π^0 production, such as the $ep\gamma_R\gamma$ or $ep\gamma_R\pi^0$ final states. Here γ_R is the photon radiated by the incoming or outgoing electron. There are also background events associated with particle misidentification and multipion production. In the fit, it is assumed that the missing mass squared distributions corresponding to single photon and single π^0 production have a Gaussian shape defined by the detector resolution. The radiative tails associated with γ and π^0 production, and the background from particle misidentification and multipion production, are fitted by a polynomial function. A sum of two Gaussians and a polynomial function is used in the final fit,

$$F = N_\gamma \cdot G_\gamma + N_{\pi^0} \cdot G_{\pi^0} + P_3 \cdot \mathrm{Pol}_3, \qquad (23)$$

where the fit parameters N_γ and N_{π^0} are the number of single photon and single pion events, respectively. The fit parameter P_3 is the relative magnitude of the background. The shape of the background, Pol_3, has been determined by a fit to the tails of the missing mass squared distribution. The mean values and the standard deviations of the Gaussian functions G_γ and G_{π^0} are determined by the fits to the missing mass squared distributions of the BH, $ep \to e'p\gamma_R$, and the single pion, $ep \to e'p\pi^0$, events. The identification of the BH and π^0 events is conducted the same way as described above. For the extraction of the Gaussian parameters, the function $f = A \cdot G_{\gamma(\pi^o)}(M_x, \sigma_x) + \mathrm{Pol}_3$ is used to fit the missing mass squared distributions of identified BH and π^0 final states individually. Here, the fit parameter A is the amplitude of the Gaussian function. The parameters M_x and σ_x are the mean value and the standard deviation of the Gaussian function. The function Pol_3, as in Eq. (23), is used to describe the radiative tail and the background under the missing mass peak. An example of a fit to the missing mass squared distribution of $ep \to epX$ for the BH events in the kinematical region $1.0 < Q^2 < 1.35$ (GeV/c)^2 and $0.1 < -t < 0.4$ (GeV/c)^2 is shown in Fig. 9(a). A fit to the M_x^2 distribution of the single pion events for the same kinematical bin is shown in Fig. 9(b). The parameters M_x and σ_x have been determined for each Q^2 and t bin.

The missing mass squared distributions for each helicity state and for the helicity sum in each kinematical bin are fitted using the function in Eq. (23). An example of a fit for a typical bin, $\phi_{p\gamma}$ from 35° to 70°, $1.0 < Q^2 < 1.35$ (GeV/c)^2, and $0.1 < -t < 0.4$ (GeV/c)^2 is shown in Fig. 10. First, a fit with a third-order polynomial is performed to the points outside of the peak region, $-0.1 < M_x^2 < -0.08$ (GeV/c)^2 and $0.12 < M_x^2 < 0.2$ (GeV/c)^2, to determine the shape of the polynomial Pol_3, see Fig. 10(a). Then, using the corresponding mean values and standard deviations of the Gaussian functions G_γ and G_{π^0}, fits to the M_x^2 distributions for the positive [Fig. 10(b)] and negative [Fig. 10(c)] beam helicity states, and for the helicity sum [Fig. 10(d)] were performed.

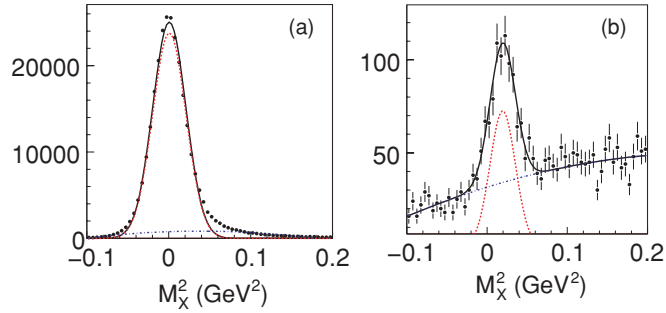

FIG. 9. (Color online) Fits to identified (a) $ep\gamma$ and (b) $ep\pi^0$ final states to determine the mean values and standard deviations of the Gaussian functions G_γ and G_{π^0}. The solid line is the fit function, the dashed line is the fitted Gaussian function, and the dashed-dotted line is the polynomial fit to the radiative tail and the background.

Fits to the M_x^2 distributions have been performed in $11\phi_{p\gamma}$ bins for each Q^2 and t bin. The extracted number of photon events are used to calculate A_{LU} for each kinematical point.

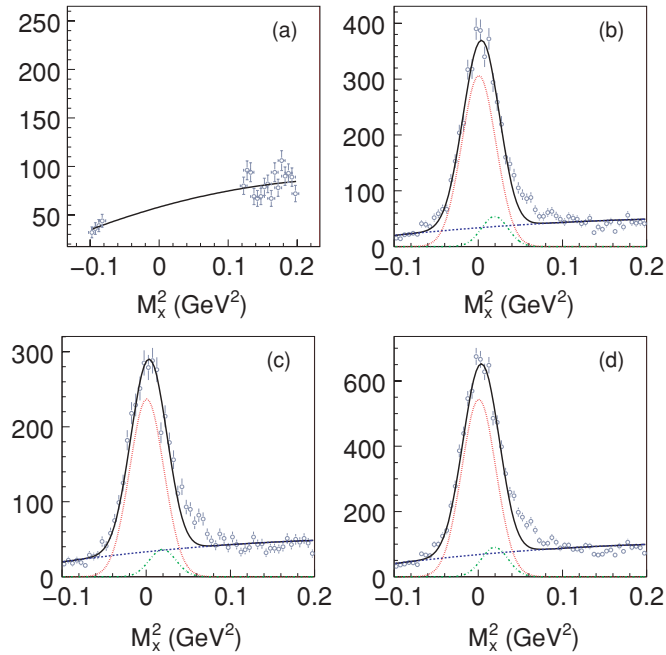

FIG. 10. (Color online) Example of fits obtained using Eq. (23) for one $\phi_{p\gamma}$ bin. (a) Fit to the background using the end points of the M_x^2 distribution. (b), (c), and (d) are fits to the M_x^2 distributions corresponding to positive, negative, and summed beam helicity states, respectively. In (b)–(d), the fit parameters are the number of single photon and π^0 events; the solid lines are the fit functions as defined in Eq. (23), the dashed lines are the Gaussian functions for the single photon events, the dashed-dotted lines are the Gaussian functions for the single π^0 events, and the dashed-dot-dot-dot lines are the polynomial background.

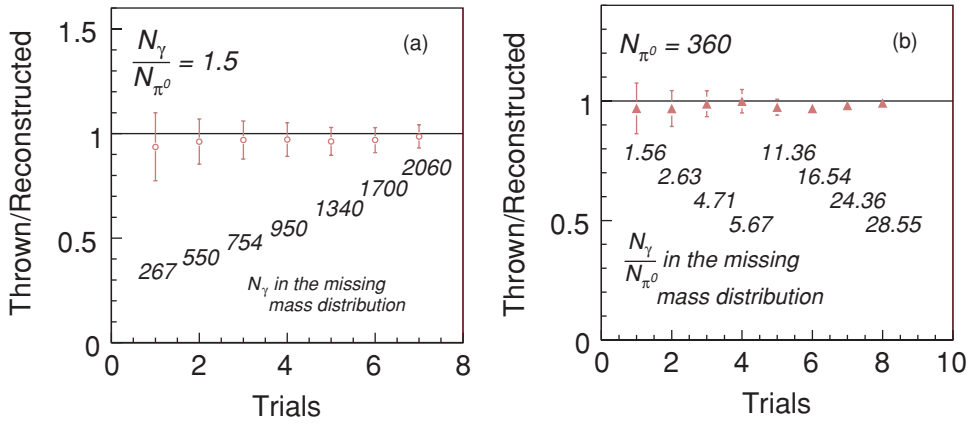

FIG. 11. (Color online) Ratios of initial to reconstructed single photon events (a) for a constant $N_\gamma/N_{\pi 0}$ ratio and (b) for a constant number of events in the mixed distribution. In (a) the numbers under each point on the plot correspond to the initial number of $ep\gamma$ events. In (b) the numbers under each point show the ratios of the $ep\gamma$ to $ep\pi^0$ events in the mixed sample.

VI. STUDIES OF THE ANALYSIS METHOD

The mean values of the missing mass squared distributions for the single photon and π^0 final states are separated by approximately one-σ of the fitted Gaussian distributions. This implies that any small systematic uncertainties in the energy calibration will directly affect the fit results. The accuracy of the determination of N_γ has been studied using real and simulated data. In both cases, single photon and π^0 events are mixed together, and the missing mass squared distributions of the mixed samples are fitted using the function in Eq. (23) to reconstruct the number of photon and pion events. The difference between the initial and the reconstructed number of photon events is taken as a measure of the uncertainty. Using the fit results to the M_x^2 distributions for the DVCS analysis as a guide, the mixed samples with different statistics and the relative ratios of the photon and pion events have been studied.

A. Studies with experimental data

The main advantages of using measured data are the correct representation of the background shape and the missing mass squared resolutions. First, separate sets of identified $ep\gamma$ and $ep\pi^0$ final states were created. The method of identification of the photon and pion final states has been explained before. The initial number of events in each final state for the mixing in a given kinematical bin was determined by using a single Gaussian and a polynomial fit to the M_x^2 distributions. Then the two samples were mixed, and the number of events in each final state in the mixed sample was then reconstructed by a fit to the line shape of the missing mass squared distribution by using the function in Eq. (23).

Two cases of event mixing were considered. In the first case, the mixing ratio of the $ep\gamma$ and $ep\pi^0$ events was kept constant at 1.5, while the total number of events in the mixed distributions was changed. The open circle points in Fig. 11(a) show the ratio of the initial number of photon events to the number of reconstructed events (from a fit to the M_x^2 distribution of mixed events). The numbers under each point on the plot correspond to the initial number of $ep\gamma$ events. Within statistical uncertainties, the reconstructed and the initial number of photon events are the same, although there is a general trend of the reconstructed numbers to be a few percent larger than the initial number.

In the second case, the number of $ep\pi^0$ events was kept constant at 360, while the number of $ep\gamma$ events increased with each trial. In Fig. 11(b), the ratio of the initial to the reconstructed number of single photon events is shown with triangular points. The numbers under each point show the ratio of the $ep\gamma$ to $ep\pi^0$ events in the mixed sample. Again, within statistical uncertainties, the ratios of the initial to reconstructed number of single photon events are consistent with unity.

The studies with mixed samples of identified photon and pion final states using the experimental data show that the number of single photon events can be reconstructed using the fit to the M_x^2 distribution with better than 5% accuracy.

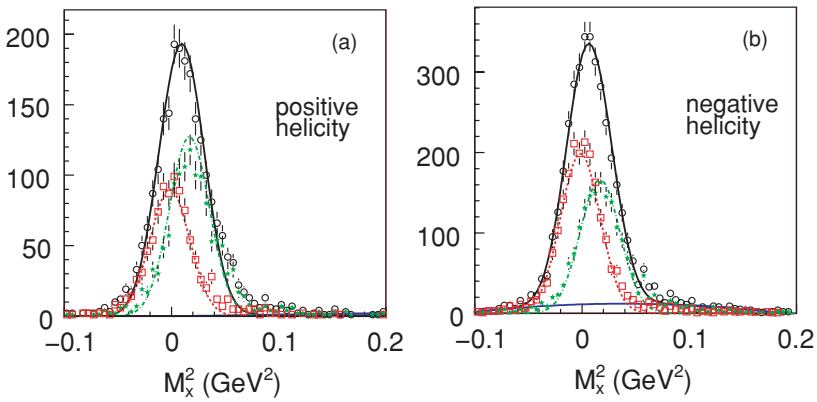

FIG. 12. (Color online) Simulated missing mass squared distributions for (a) positive and (b) negative helicity for one $\phi_{p\gamma}$, Q^2, and t bin. The open circles with error bars correspond to the mixed event distributions. The solid line is the fit using the function in Eq. (23) to these points. The open squares represent the M_x^2 distributions of the initial photon events. The dashed lines are the resulting G_γ from the fit to the mixed distributions. The stars and dashed-dotted lines are the same for the single pion final state. The dashed-dot-dot-dotted line in (b) corresponds to the fitted polynomial background.

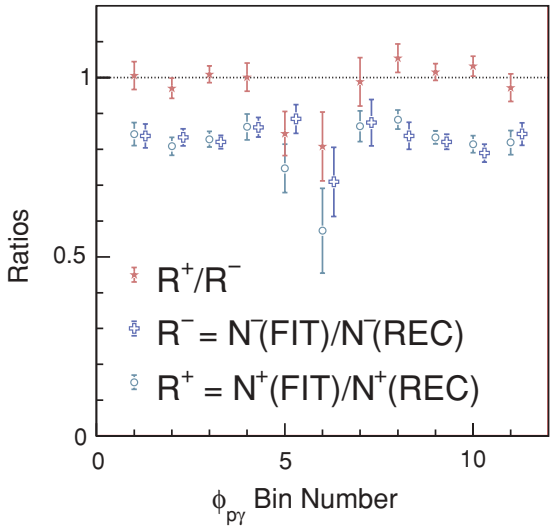

FIG. 13. (Color online) $\phi_{p\gamma}$ dependence of ratios of the number of single photon events extracted using the fits to the missing mass squared distribution of the mixed events to the number of single photon events that passed the analysis cuts for the positive (open circles) and negative (crosses) beam helicity states. The stars represent the ratio of the two ratios.

B. Studies with simulated data

Another set of tests was performed using a realistic event generator [22] for the $ep \to ep\gamma$ and $ep \to ep\pi^0$ reactions. The response of the CLAS detector was simulated using a GEANT-based program. The simulated data were processed with the same event reconstruction and physics analysis algorithms that were used for the measured data. Events from both samples (that passed all analysis cuts) in a given kinematical bin were mixed together, and fits to the line shape of the M_x^2 distributions of the mixed events were performed to extract the number of single photon and single π^0 final states.

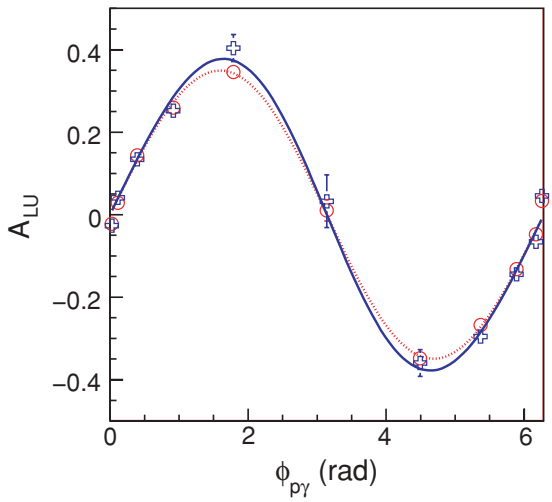

FIG. 14. (Color online) Simulated and extracted A_{LU}. The crosses are the extracted asymmetries and the solid line is the fit to these points using the function in Eq. (22). The open circles and the dotted line are the same for the simulated asymmetry.

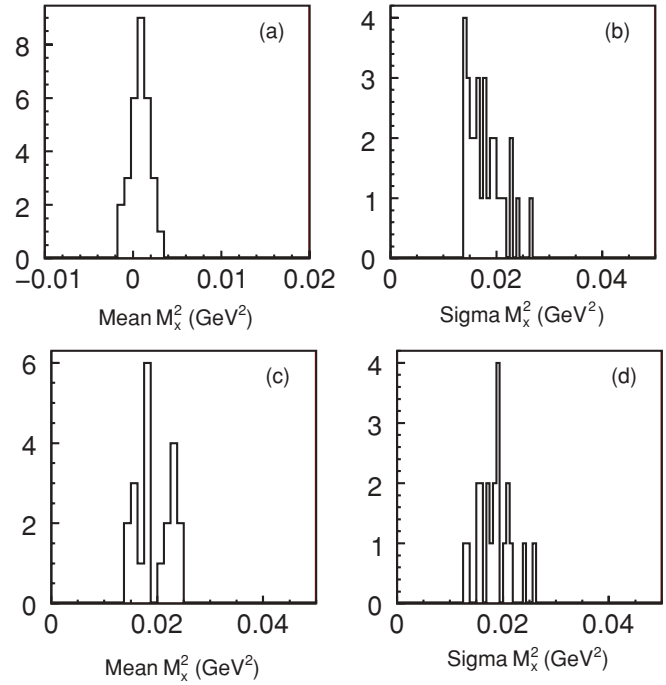

.

FIG. 15. Distribution of the means and standard deviations of the Gaussian functions for the photon and pion peaks for sub-bins of one kinematical bin: $1.7 < Q^2 < 2.8$ (GeV/c)^2 and $0.1 < |t| < 0.8$ (GeV/c)^2.

The parameters for G_γ and G_{π^0} were derived from the fits to the missing mass squared distributions of the $ep \to ep\gamma$ and $ep \to ep\pi^0$ events before mixing, respectively.

Examples of the fits to the M_x^2 distributions for the different helicity states of the simulated data are shown in Fig. 12.

In Fig. 13, the ratio of the number of single photon events, obtained from fits to the missing mass squared distributions of the mixed event sample, to the number of reconstructed photon events that passed all analysis cuts are shown for all $\phi_{p\gamma}$ bins at $1.0 < Q^2 < 1.35$ (GeV/c)^2 and $0.1 < t < 0.4$ (GeV/c)^2.

TABLE I. Calculated beam spin asymmetry A_{LU} at each $\phi_{p\gamma}$ for three Q^2 bins, see Fig. 7. The average values of x_B and t are shown in Table III.

$\langle Q^2 \rangle$	1.22 (GeV/c)^2		1.51 (GeV/c)^2		2.04 (GeV/c)^2	
$\langle \phi \rangle$	A_{LU}	δA_{LU}	A_{LU}	δA_{LU}	A_{LU}	δA_{LU}
1.5°	−0.0051	0.0056	0.0007	0.0055	0.0021	0.0060
6.5°	0.0289	0.0139	−0.0005	0.0134	0.0315	0.0154
22.5°	0.0794	0.0221	0.0660	0.0196	0.1054	0.0217
52.5°	0.1427	0.0381	0.1826	0.0322	0.1544	0.0454
102.5°	0.2028	0.0589	0.2080	0.0475	0.2237	0.0750
180.0°	0.0227	0.1062	0.0703	0.1146	0.0071	0.1307
257.5°	−0.1394	0.0582	−0.2592	0.0539	−0.1471	0.0906
307.5°	−0.1662	0.0431	−0.2173	0.0337	−0.1451	0.0463
337.5°	−0.0862	0.0203	−0.0631	0.0185	−0.0643	0.0220
353.5°	−0.0147	0.0135	0.0130	0.0129	−0.0308	0.0158
358.5°	−0.0032	0.0063	−0.0001	0.0058	0.0006	0.0063

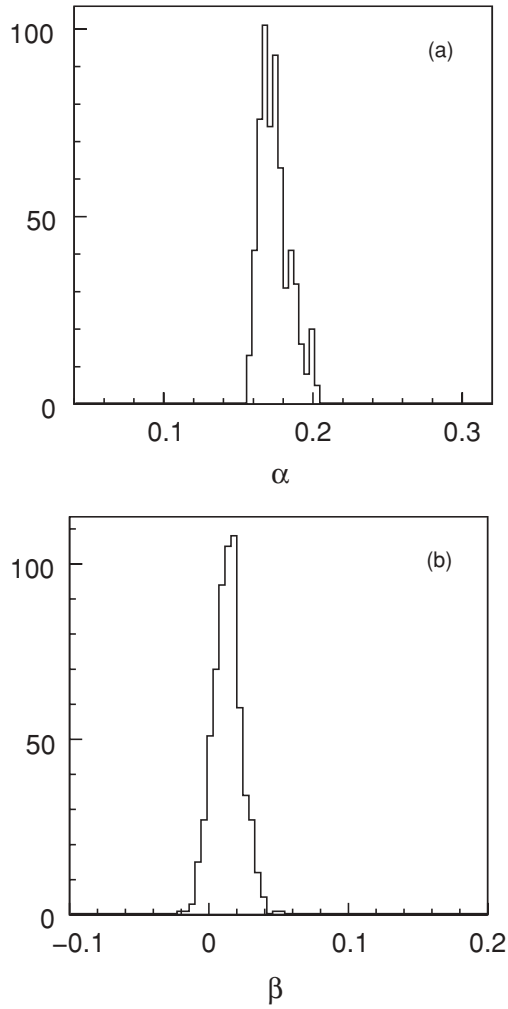

FIG. 16. Distribution of the (a) $\sin\phi_{p\gamma}$ and (b) $\sin 2\phi_{p\gamma}$ moments of the beam spin asymmetries for the Q^2 bin of 1.35–1.7 $(\mathrm{GeV}/c)^2$ and $0.1 < |t| < 0.4$ $(\mathrm{GeV}/c)^2$, extracted from the fits to the missing mass squared distributions using different values of means and standard deviations of G_γ and G_{π^0} within ± 1 rms.

TABLE II. Calculated beam spin asymmetry, A_{LU}, at each $\phi_{p\gamma}$ for three t bins, see Fig. 7. The average values of x_B and Q^2 are shown in Table IV.

$\langle -t\rangle$	0.19 $(\mathrm{GeV}/c)^2$		0.30 $(\mathrm{GeV}/c)^2$		0.46 $(\mathrm{GeV}/c)^2$	
$\langle\phi\rangle$	A_{LU}	δA_{LU}	A_{LU}	δA_{LU}	A_{LU}	δA_{LU}
1.5°	0.0014	0.0102	−0.0002	0.0071	0.0141	0.0049
6.5°	0.0449	0.0219	0.0024	0.0185	0.0209	0.0131
22.5°	0.0298	0.0260	0.1143	0.0266	0.0969	0.0204
52.5°	0.1354	0.0402	0.1871	0.0503	0.1998	0.0450
102.5°	0.2361	0.0503	0.1191	0.0906	0.2461	0.0984
180.0°	−0.0858	0.1092	0.1608	0.1994	0.0629	0.1908
257.5°	−0.2164	0.0533	−0.0513	0.1210	−0.3280	0.1797
307.5°	−0.2105	0.0389	−0.1756	0.0548	−0.1679	0.0515
337.5°	−0.0691	0.0253	−0.0594	0.0260	−0.0653	0.0194
353.5°	0.0111	0.0218	0.0010	0.0179	−0.0377	0.0129
358.5°	0.0075	0.0110	−0.0035	0.0076	0.0045	0.0053

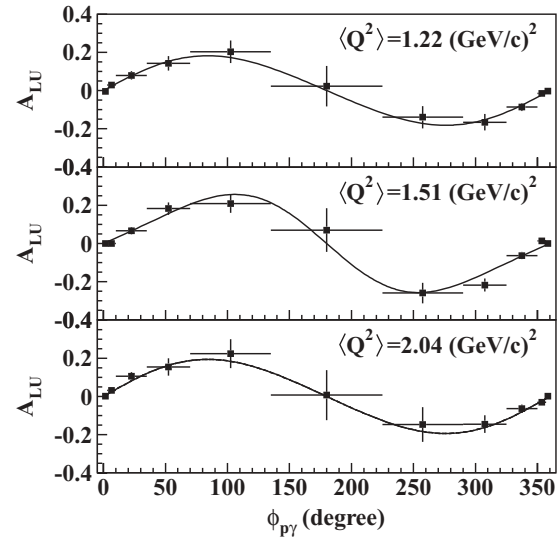

FIG. 17. Asymmetry A_{LU} as a function of azimuthal angle fitted according to Eq. (22) to extract the $\sin\phi$ and $\sin 2\phi$ moments in three Q^2 bins, see Table III.

The crosses and the circles represent the ratios for different helicities. The stars show the ratio of these ratios. The extracted number of events by the fit is always lower than the number of events in the mixed sample by about 20%. This is because there is no background or radiative effects in the simulated data, while the fit procedure finds a nonzero contribution for the polynomial function at the expense of the photon and pion events. The important information is indicated by the stars, which show that for each $\phi_{p\gamma}$ bin, these ratios are the same for both helicities.

In Fig. 14, the beam spin asymmetry, as defined in Eq. (18), is presented as a function of $\phi_{p\gamma}$. The simulated $\phi_{p\gamma}$ dependence of the asymmetry is shown with circles.

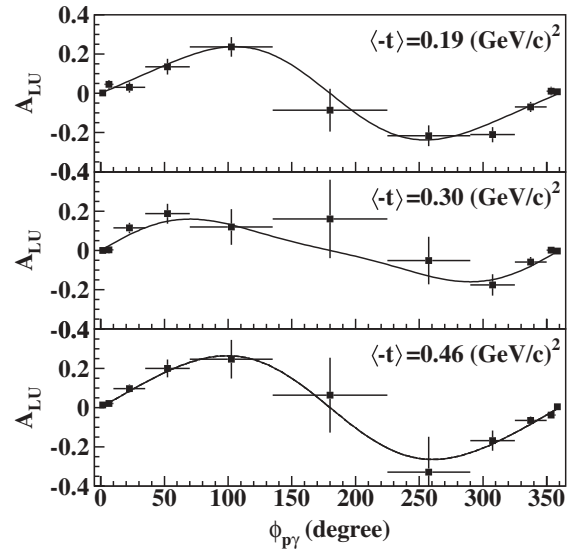

FIG. 18. Asymmetry A_{LU} as a function of azimuthal angle fitted according to Eq. (22) to extract the $\sin\phi$ and $\sin 2\phi$ moments in three t bins, see Table IV.

TABLE III. Results from the fits to the ϕ dependences of A_{LU} with the functions presented in Eqs. (19) and (22). Only statistical uncertainties are presented.

$\langle Q^2\rangle$ [(GeV/c)^2]	$\langle x_B\rangle$	$\langle -t\rangle$ [(GeV/c)^2]	α	β	α'	γ
1.22	0.17	0.23	0.181 ± 0.032	0.099 ± 0.023	0.181 ± 0.032	-0.098 ± 0.228
1.51	0.20	0.26	0.245 ± 0.028	-0.040 ± 0.021	0.234 ± 0.024	0.319 ± 0.195
2.04	0.28	0.38	0.192 ± 0.044	0.010 ± 0.030	0.191 ± 0.045	-0.107 ± 0.288

The crosses represent the asymmetry obtained using the fit procedure. The solid line is a fit using the function in Eq. (22) to the extracted asymmetry. The dotted line is a fit to the simulated asymmetry. The $\sin\phi_{p\gamma}$ moment for the extracted asymmetry is approximately 3% higher than the simulated moment. This difference is used as the systematic uncertainty in the determination of the moments of the azimuthal asymmetry in DVCS.

C. Dependences on the parameters of G_γ and G_{π^0}

Additional sources of systematic uncertainties are the dependences of the mean values and standard deviations of the functions G_γ and G_{π^0} on the kinematics of an event. In Fig. 15, distributions of these parameters obtained in smaller sub-bins of t and Q^2 within the Q^2 bin of 1.7–2.8 (GeV/c)^2 and the t bin of 0.1–0.8 (GeV/c)^2 are shown. Single photon (Bethe-Heitler events, selected as shown in Fig. 5) events in this t and Q^2 bin were divided into 30 sub-bins [Figs. 15(a) and 15(b)], while single pion events were divided into 21 sub-bins [Figs. 15(c) and 15(d)]. Physics asymmetries in each t and Q^2 bin were extracted using the central values of these parameters in the given bin. To estimate the systematic uncertainties, the whole fitting procedure was repeated with additional four values of these parameters within a ± 1 rms range. Thus, a total of $5^4 = 625$ different sets of means and standard deviations were tested for each t and Q^2 bin.

In Fig. 16(a), the distribution of the $\sin\phi_{p\gamma}$ moments obtained for different sets of Gaussian parameters is shown for the Q^2 and t bin of 1.35–1.7 (GeV/c)^2 and 0.1–0.4 (GeV/c)^2, respectively. The rms of this distribution is 0.015. The same distribution for the $\sin 2\phi_{p\gamma}$ moment has an rms of 0.013, see Fig. 16(b). These rms values were taken as the systematic uncertainties of the moments due to the kinematical dependence of the parameters of G_γ and G_{π^0} within the kinematic bin.

VII. RESULTS

Our results on the beam spin asymmetry, calculated using Eq. (18), are presented in Tables I and II. To extract $\sin\phi_{p\gamma}$ (α) moments as a function of Q^2 and t, the azimuthal angular dependence of A_{LU} was fitted with the function presented in Eq. (22). In Fig. 17, the $\phi_{p\gamma}$ dependences of A_{LU} for three bins of Q^2 for $0.1 < -t < 0.4$ (GeV/c)^2 are shown. The azimuthal angular dependence of A_{LU} for three bins of t at $1.4 < Q^2 < 2.5$ (GeV/c)^2 is shown in Fig. 18. The solid line is a fit to the measured asymmetries using the function presented in Eq. (22) in order to extract $\sin\phi$ (α) and $\sin 2\phi$ (β) moments. In both figures only statistical uncertainties are shown.

The systematic uncertainties on α have been evaluated using the studies presented in the previous section. Besides the systematic uncertainties due to the M_x^2 fits, 3%, and the determination of the parameters of G_γ and G_{π^0}, $\pm 8\%$, there is an uncertainty in the calculation of the A_{LU} from the determination of the beam polarization, P_e, and an uncertainty due to the charge asymmetry. The uncertainty on the beam polarization was estimated to be $\pm 3\%$. The helicity-dependent charge asymmetry was about 0.7%. The estimated total systematic uncertainties for the extracted moments are -8.7% and $+8.2\%$.

The final results on the moments α and β are presented in Tables III and IV. For consistency checks, the $\phi_{p\gamma}$ dependence of the A_{LU} were fitted with the function presented in Eq. (19). The obtained results on α' and γ are also presented in Tables III and IV. In the tables, only the statistical uncertainties are quoted.

In Fig. 19, the Q^2 and t dependences of the $\sin\phi_{p\gamma}$ moment (α) are shown. In the graph for the Q^2 dependence, the previously published CLAS result on α [14] is shown by an open cross. The solid and dashed-dotted lines are the Q^2 and t dependences of the $\sin\phi_{p\gamma}$ moments of the beam spin asymmetry calculated using a Regge trajectory exchange model for the interaction of the photon with the proton [23,24] using two treatments of the unitarity cuts. The dashed-dotted curves retain the contribution of the poles [23]

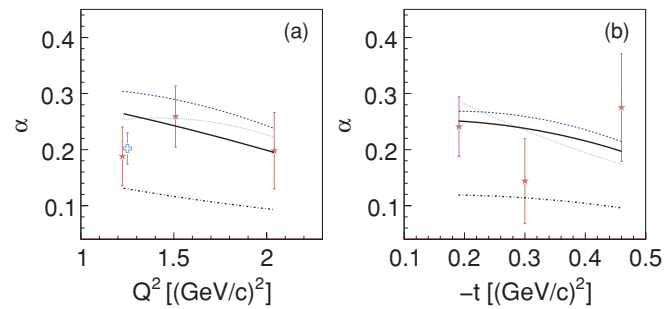

FIG. 19. (Color online) (a) Q^2 and (b) t dependences of the $\sin\phi_{p\gamma}$ moments of the DVCS asymmetry. The cross symbol is the asymmetry measured by CLAS with the 4.2 GeV data. The curves are model calculations based on a Regge model for the photon-proton interaction (solid and dashed-dotted lines) [24] and on the GPD-based model (dashed and dotted lines) [25,29]. Each curve represents different parameter settings (see text for details). In the plots the error bars are the combined statistical and systematical uncertainties added in quadrature.

TABLE IV. Results from the fits to the ϕ dependences of A_{LU} with the functions presented in Eqs. (19) and (22). Only statistical uncertainties are presented.

$\langle -t \rangle$ [(GeV/c)^2]	$\langle x_B \rangle$	$\langle Q^2 \rangle$ [(GeV/c)^2]	α	β	α'	γ
0.19	0.23	1.69	0.228 ± 0.029	-0.034 ± 0.024	0.222 ± 0.026	0.318 ± 0.248
0.30	0.23	1.74	0.147 ± 0.055	0.033 ± 0.037	0.161 ± 0.045	-0.223 ± 0.274
0.46	0.25	1.83	0.260 ± 0.062	-0.022 ± 0.039	0.260 ± 0.057	0.200 ± 0.331

and the contribution of the ρ-p elastic cut [24]. They take into account the coupling between the γ-p and the ρ-p channels and are well under control since they rely on known on-shell matrix elements. The solid curves also take into account all of the inelastic diffractive cuts, under the assumption that diffractive dissociation saturates the photoabsorption cross section. This treatment leads to an excellent agreement with the unpolarized cross sections, as well as the helicity difference of the DVCS cross sections, recently measured in Hall A [17].

The other two curves in the graphs represent calculations of the $\sin\phi_{p\gamma}$ moments with a GPD-based model [25], using a Regge ansatz for the t distribution of the GPD [26]. The parametrization of GPDs includes the D term (to ensure the polynomiality of Mellin moments of GPDs [27]). Helicity-dependent cross sections were calculated at the twist-3 level and include target mass corrections [25]. Calculations are done for two different skewedness parameter values for sea quarks, $b_{\rm sea} = 1$ (dashed line) and $b_{\rm sea} = 2$ (dotted line). In the calculations, the profile parameter for the valence quark was $b_{\rm val} = 1$ and the Regge slope parameter $\alpha' = 1.05$ [26]. The data favor the GPD model with the sea quark skewedness parameter $b_{\rm sea} = 2$. The calculations include the DVCS contributions to both the numerator [Eq. (13)] and denominator [Eq. (12)] of A_{LU}.

In the method used for separation of the single photon events, the radiative tails were folded into the "background." The radiative effects are inseparable from the Born level $ep \to e'p\gamma$ process. Detailed radiative calculations by Vanderhaeghen *et al.* [28] showed that the effect on the beam spin asymmetry is less than 5%. This is much smaller than the uncertainties of our measurements.

The extracted $\sin 2\phi_{p\gamma}$ moment or $\cos\phi_{p\gamma}$ denominator term of A_{LU} is within uncertainties consistent with zero. The precision of our results is not good enough to determine small contributions from higher twists and the power-suppressed terms.

VIII. SUMMARY

The beam spin asymmetry A_{LU} in the deeply virtual production of real photons has been measured using a 4.8 GeV longitudinally polarized electron beam and the CLAS detector. The experimental A_{LU} for each kinematical bin was calculated using the number of single photon events extracted from the fits to the line shape of the missing mass squared (M_x^2) distributions. Studies using Bethe-Heitler and π^0 production events have been performed to test the validity of the fit method. It was found that the systematic uncertainties on the moments from the fit procedure are not more than 6%. Overall systematic uncertainties have been estimated to be less than 9% of the value of α.

The $\sin\phi_{p\gamma}$, $\sin 2\phi_{p\gamma}$, and $\cos\phi_{p\gamma}$ moments of the azimuthal angular dependence of the asymmetry have been extracted in three bins of Q^2 and three bins of transferred momentum t (see Tables III and IV). The Q^2 and t dependences of the $\sin\phi_{p\gamma}$ moment are compared with theoretical calculations using the GPD-based model for DVCS [25,29] and the photon-proton interaction based on a Regge model [24]. The sensitivity of our results is not good enough to estimate small contributions from higher twists and the power-suppressed terms. However, the data put constraints on the model parameters used to calculate the beam spin asymmetry. Also, the data are reproduced by a model based on Regge poles and unitary cuts. Whether this is a consequence of the quark hadron duality remains to be investigated. Clearly, more data in a wide range of kinematics are needed to refine the parameters of the models. New experiments on DVCS and on deeply virtual meson production will provide further observables in the deeply exclusive production regime that can be used in a global fit to extract the GPDs.

ACKNOWLEDGMENTS

We acknowledge the outstanding work of the staff of the Accelerator Division and the Physics Divisions, and the Hall B technical staff that made this experiment possible. We also acknowledge M. Vanderhaeghen for his useful discussions and for providing a computer code for the model calculations. This work was supported in part by the Istituto Nazionale di Fisica Nucleare, the French Centre National de la Recherche Scientifique, the French Agence Natioanale de la Recherche, the French Commissariat à l'Energie Atomique, the US Department of Energy, the National Science Foundation, and the Korea Research Foundation. Authored by The Southeastern Universities Research Association, Inc., under US DOE Contract No. DE-AC05-84150.

[1] J. Gronberg *et al.* (CLEO Collaboration), Phys. Rev. D **57**, 33 (1998).

[2] A. P. Bakulev, K. Passek-Kumericki, W. Schroers, and N. G. Stefanis, Phys. Rev. D **70**, 033014 (2004).

[3] A. V. Belitsky, X. Ji, and Feng Yuan, Phys. Rev. Lett. **91**, 092003 (2003).

[4] X. Ji, Phys. Rev. Lett. **78**, 610 (1997); Phys. Rev. D **55**, 7114 (1997).

[5] A. V. Radyushkin, Phys. Lett. **B380**, 417 (1996); Phys. Rev. D **56**, 5524 (1997).
[6] J. C. Collins, L. Frankfurt, and M. Strikman, Phys. Rev. D **56**, 2982 (1997).
[7] M. Burkardt, Phys. Rev. D **62**, 071503(R) (2000).
[8] A. Belitsky, D. Muller, and A. Kirchner, Nucl. Phys. **B629**, 323 (2002).
[9] D. Muller (private communication).
[10] M. Diehl, T. Gousset, B. Pire, and J. P. Ralston, Phys. Lett. **B411**, 193 (1997).
[11] K. Goeke, M. Poliakov, and M. Vanderhaeghen, Prog. Part. Nucl. Phys. **47**, 401 (2001).
[12] M. Diehl, Phys. Rep. **41**, 388 (2003).
[13] M. Burkardt, Int. J. Mod. Phys. A **18**, 173 (2003).
[14] S. Stepanyan *et al.*, Phys. Rev. Lett. **87**, 182002 (2001).
[15] A. Airapetian *et al.*, Phys. Rev. Lett. **87**, 182001 (2001).
[16] S. Chen *et al.*, Phys. Rev. Lett. **97**, 072002 (2006).
[17] C. Munoz Camacho *et al.*, Phys. Rev. Lett. **97**, 262002 (2006).
[18] A. Airapetian *et al.*, Phys. Rev. D **75**, 011103 (2007).
[19] A. Airapetian *et al.*, J. High Energy Phys. 06 (2008) 066.
[20] F. X. Girod *et al.*, Phys. Rev. Lett. **100**, 162002 (2008).
[21] B. A. Mecking *et al.*, Nucl. Instrum. Methods A **503**, 513 (2003).
[22] H. Avakian (private communication).
[23] F. Cano and J.-M. Laget, Phys. Lett. **B551**, 317 (2003); **B571**, 260(E) (2003).
[24] J.-M. Laget, Phys. Rev. C **76**, 052201(R) (2007).
[25] M. Vanderhaeghen, P. A. M. Guichon, and M. Guidal, Phys. Rev. D **60**, 094017 (1999).
[26] M. Guidal, M. V. Polyakov, A. V. Radyushkin, and M. Vanderhaeghen, Phys. Rev. D **72**, 054013 (2005).
[27] A. V. Radyushkin, Phys. Rev. D **59**, 014030 (1998).
[28] M. Vanderhaeghen, J. M. Friedrich, D. Lhuillier, D. Marchand, L. VanHoorebeke, and J. VandeWiele, Phys. Rev. C **62**, 025501 (2000).
[29] K. Goeke, M. V. Polyakov, and M. Vanderhaeghen, Prog. Part. Nucl. Phys. **47**, 401 (2001).